Integration of microfiltration and visible-light-driven photocatalysis on g-C₃N₄ nanosheet/reduced graphene oxide membrane for enhanced water treatment

Huanxin Zhao [a,b], Shuo Chen [a], Xie Quan [a,*], Hongtao Yu [a], Huimin Zhao [a]

[a] Key Laboratory of Industrial Ecology and Environment Engineering (Ministry of Education, China), School of Environmental Science and Technology, Dalian University of Technology, Dalian 116024, China
[b] School of Environmental and Safety Engineering, Shenyang University of Chemical Technology, Shenyang 110142, China

A B S T R A C T

A graphitic carbon nitride nanosheet/reduced graphene oxide/cellulose acetate composite photocatalytic membrane (g-C₃N₄ NS/RGO/CA) was fabricated by assembling a g-C₃N₄ NS/RGO photocatalyst on the surface of commercial CA membrane. Owing to the attractive photocatalytic efficiency of g-C₃N₄ NS under visible light irradiation and photogenerated charge separation resulting from the unique hetero-structure between g-C₃N₄ NS and RGO, g-C₃N₄ NS/RGO/CA composite photocatalytic membranes exhibited superior performance in water treatment under visible light irradiation. The removal efficiency of Rhodamine B by the integrated process of filtration and visible light driven photocatalysis was four times that of membrane filtration alone. The integrated process also displayed efficient inactivation of *Escherichia coli* at three orders of magnitude higher than that of filtration alone. The permeate flux for the integrated process was 3.7 times that of filtration alone, suggesting its good anti-fouling property under visible light irradiation. The integrated system was employed to treat surface water and evaluate its performance in real water treatment. The integrated process showed much better efficiencies for the removal of COD$_{Mn}$, TOC, UV$_{254}$, and bacteria from surface water than those of membrane filtration alone. This work gives insight to the effective application of solar energy for the improvement of membrane separation in water treatment.

© 2016 Elsevier B.V. All rights reserved.

1. Introduction

Efficient, safe and cost-effective processes for water treatment are highly desired yet still a challenge [1,2]. Membrane filtration with the advantages of quick separation of pollutants and low environmental impact has attracted much attention [3,4]. In particular, microfiltration have been acknowledged as a promising technology for water purification because of the high yield of production and low energy consumption [5,6]. Nevertheless, widely used microfiltration membrane based on a size exclusion have limitations in removing many organic contaminants with smaller sizes than its pores during the simple separation process, resulting in the effluent water with potential hazard. Moreover, the inherent membrane fouling, which leads to a high permeate loss and energy cost, also restricts its application [7,8].

To overcome these drawbacks, the integration of membrane filtration with photocatalysis, in which a membrane is functionally modified with a photocatalytic layer, has been proposed. Zhang et al. [9] and Choi et al. [10] reported the fabrication of photocatalytic membrane by the immobilization of TiO₂ photocatalyst on the surface of ceramic membrane for water treatment. During this integrated process, photocatalytic degradation of organic contaminants prevents them from permeating through the membrane without treatment. Simultaneously, the inherent membrane fouling can be mitigated because of the efficient decomposition of pollutants by photocatalysis. Despite of these advantages, the photocatalytic membrane still faces some crucial issues. For instance, the photocatalytic materials for the functional layer are mainly focused on TiO₂ based photocatalysts [11,12], which suffer from limited performance because of the fast recombination of photogenerated charges. Moreover, TiO₂ exhibits poorly photoactivity in the visible light region which greatly limits its practical applications. Furthermore, because of the degradation of conventional polymer membrane under UV light irradiation, expensive ceramic membranes with good tolerance to UV light are employed as the

---

* Corresponding author.
 E-mail address: quanxie@dlut.edu.cn (X. Quan).

supporting layer [9–11], which results in the high cost of membrane products. The limited performance, poor visible light response and high cost of preparation for photocatalytic membranes do not meet the applicable requirements.

Developing a high performance visible light driven photocatalyst which can be modified on the surface of polymer membrane is an effective strategy to solve the problems aforementioned. Among photocatalysts with visible light response, graphitic carbon nitride (g-C_3N_4) is especially attractive because of its visible light response and excellent chemical stability [13,14]. Although g-C_3N_4 has been reported for photocatalytic water splitting [13], CO_2 reduction [15] and organic contaminants degradation [14], its low photocatalytic efficiency resulting from the fast recombination of photogenerated charges weakens its photocatalytic activity. Recently, researchers found that exfoliating bulk g-C_3N_4 into ultra-thin two-dimensional (2D) g-C_3N_4 nanosheets (g-C_3N_4 NS) is an effective strategy to enhance its photocatalytic efficiency by improving the mobility and density of the photogenerated charges [16,17]. However the photocatalytic efficiency remains far from satisfaction on modifying membrane for water treatment.

In this study, to improve the photocatalytic efficiency of g-C_3N_4 NS, reduced graphene oxide (RGO) which is widely used as an electron acceptor to facilitate photogenerated charge separation [18] was employed. The g-C_3N_4 NS/RGO composite photocatalyst was assembled on a commercial cellulose acetate (CA) membrane by vacuum filtration and high-pressure process. Apart from the photogenerated charge separation, RGO, which also has a 2D nanosheet structure, is helpful to improve the flexibility of the membrane by connecting the individual g-C_3N_4 NS. Because of the visible light response of g-C_3N_4 NS/RGO composite, the low cost commercial CA membrane can be employed as the supporting layer instead of expensive ceramic membranes. The present work describes a novel photocatalytic membrane with visible light response, considerable photocatalytic activity and low preparation cost, with promising application to water treatment.

2. Experimental

2.1. Chemicals and materials

Potassium permanganate ($KMnO_4$), graphite powder, melamine and sulfuric acid (H_2SO_4, 98%) were obtained from Kemiou Chemical Reagent Co. Ltd. (Tianjin, China). Absolute ethanol was supplied by Sinopharm Chemical Reagent Co. Ltd. (Shanghai, China). Other chemicals were purchased from J&K Chemical Co. Ltd. (Beijing, China). All the chemicals were analytical reagent without any further purification. CA membrane was purchased from Millipore Co. Ltd. Polystyrene (PS) microspheres with different diameters were obtained from SmartyNano Tech. Co. Ltd. (Suzhou, China). P25 TiO_2 was obtained from Degussa Co. Ltd. Ultrapure water was prepared in the laboratory using a MilliQ SP reagent water system from Millipore Co. Ltd.

2.2. Fabrication of g-C_3N_4 NS/RGO photocatalyst

Bulk g-C_3N_4 was fabricated by directly heating melamine. g-C_3N_4 NS was fabricated by the thermal exfoliation of bulk g-C_3N_4 [19]. GO was prepared with the modified Hummer's method [18]. g-C_3N_4 NS/RGO composite photocatalyst was synthesized through a photoreduction process. (more details see supporting information)

2.3. Assembly of g-C_3N_4 NS/RGO/CA composite membrane

100 mg of g-C_3N_4 NS/RGO composite was dispersed in 200 mL pure water (Millipore, 18 MΩ cm) under assistance of ultrasonification. Then 20, 50, 100, 150 and 200 mL of the suspension were

filtrated on a piece of commercial CA membrane (47 mm in diameter and 0.45 μm in pore size) respectively. Finally, the membrane was pressed under N_2 gas of 0.5 MPa for 1 h. The control membranes of g-C_3N_4 NS/CA and P25/CA were prepared by the same method but filtrating the suspensions of g-C_3N_4 NS and P25 on the CA membrane. The mass of both g-C_3N_4 NS and P25 were the same as that of RGO/g-C_3N_4 nanosheet.

2.4. Characterization

The morphologies of both g-C_3N_4 NS/RGO composite and g-C_3N_4 NS/RGO/CA membrane were observed by field-emission scanning electron microscope (FE-SEM, S4800, Hitachi), transmission electron microscope (TEM, Tecnai G^2S-Twin) and atomic force microscope (AFM, Agilent PicoPlus) respectively. X-ray diffraction (XRD) was carried out on a X-ray diffractometer (Shimadzu XRD-6000) with Cu-Kα radiation (λ = 0.154060 nm) at a scanning speed of 4° min^{-1} in the 2θ range from 10 to 50°. Fourier transform spectrophotometer (FT-IR, VERTEX 70, Bruker) was used to characterize the functional groups with KBr as the reference sample. UV–vis absorption spectra were recorded on a Shimadzu UV-2450 spectrophotometer. Raman spectra were recorded by a Renishaw Micro-Raman system 2000 spectrometer with He-Ne laser excitation (wavelength 623.8 nm). The Brunauer-Emmet-Teller (BET) specific surface area of the sample was determined by nitrogen adsorption-desorption isotherm measurements at 77 K using Quantachrome SI system. The pore size distribution was calculated from the desorption branch of the isotherm according to the Barrett-Joyner-Halenda (BJH) model. The photoluminescence (PL) spectra were recorded on a Hitachi F-4500 spectrometer. More details about the experiments of characterization were described in the supporting information.

2.5. Measurement of mechanical strength

Ultrasonic vibration measurement was carried out to evaluate the adhesion strength between photocatalyst and CA membrane substrate. The assembling membranes were immersed in water inside a beaker, and then treated in an ultrasonic bath (50 W) for 0.5–30 min. The weight loss of the composite membrane was measured after dry.

2.6. Measurement of pore size and pure water flux

To evaluate the pore size of the membrane, the rejection rates of PS microspheres with series of diameters were determined by measuring the concentration ratios of permeated solution to feed solution. The concentration of PS was determined by measuring the absorbance at 225 nm [20]. This process was operated under the pressure of 0.05 MPa. The pure water flux was measured with a lab-scale dead-end filtration system by weighting permeate mass with an analytical balance.

2.7. Photocatalytic experiments

The photocatalytic efficiencies of g-C_3N_4 NS/RGO composite with different RGO contents were evaluated by degradation of Rhodamine B (RhB) in a quartz reactor. The initial concentration of RhB was 10 mg L^{-1} and 5 mg of photocatalyst was suspended in 100 mL RhB solution. At certain time intervals of visible light irradiation (Xe lamp, 100 mW cm^{-2}, λ > 400 nm, the optical characterization of UV filter and the spectra of the Xe lamp were supplied in Figs. S1 and S2 respectively. The light intensity was measured by radiometers (Photoelectric Instrument Factory Beijing Normal University)), 2 mL of the reaction solution was collected and centrifuged to remove the photocatalyst for analysis. The concentration of RhB

was measured by UV–vis spectrophotometer (UV-7504, Xinmao) at 554 nm.

Photocatalytic activity of the g-C$_3$N$_4$ NS/RGO/CA membrane was tested by photo-degradation of RhB imprint on the membrane surface. 50 μL of RhB with the concentration of 5 mg L^{-1} was dripped on the surface of membrane, forming a red imprint. The membrane with the red imprint was exposed to the Xe lamp irradiation for 1 min. An optical filter was used to cut off the light whose wavelength was shorter than 400 nm. The control membranes of g-C$_3$N$_4$ NS/CA and P25/CA were tested under the same condition.

2.8. Membrane performance tests

All the performance tests were carried out in a dead-end membrane filtration system (Fig. S3). RhB and Bisphenol A (BPA) were used as model contaminants to investigate the performance of the membrane for removing organic contaminants which are difficult to be removed by micro- or ultrafiltration membrane through size-exclusion. The concentration of the RhB and BPA in feed water was 5 and 10 mg L^{-1} respectively. The integrated process (membrane filtration and photocatalysis) was operated under a trans-membrane pressure of 0.05 MPa and visible light irradiation (λ > 400 nm) with the intensity of 100 mW cm^{-2}. The concentration of BPA was determined by high performance liquid chromatography (Shimadzu, LC10A HPLC). The C18 column was used and the analysis was carried out with a mobile phase of 40/44/8/8 (V/V) methanol/water/acetonitrile/tetrahydrofuran at the flow rate of 1.0 mL min^{-1}. Removal of *Escherichia coli* (*E. coli*) by the composite membrane was carried out to illustrate its capability of inactivation and anti-biofouling. The concentrations of *E. coli* in feed and permeated water were measured using the standard plate count method [21] (more details see supporting information). NaCl was added into the feed water that contained *E. coli* and its concentration was adjusted at 0.9%. The investigation of real water treatment for the composite membrane towards a real surface water from reservoir near Dalian city was carried out under the same operational conditions (pressure and light irradiation). The total organic carbon (TOC) was measured by a TOC analyzer (TOC-V$_{CPH}$, Shimadzu, Japan). UV absorbance of surface water samples at 254 nm (UV$_{254}$) were measured using UV–vis spectrophotometer. Chemical oxygen demand (COD$_{Mn}$) was determined by the method of potassium permanganate [22].

3. Results and discussion

3.1. Characterization of the composite photocatalyst

The morphology of the composite was observed by FE-SEM, TEM and AFM. The SEM image of the composite photocatalyst displayed lamellar nanosheets with a number of curves (Fig. 1a), and the TEM exhibited the expected layered morphology with many chiffon-like ripples and wrinkles (Fig. 1b). The different morphologies of g-C$_3$N$_4$ NS and RGO in the composite were distinguished by a high magnification image of TEM. As shown in Fig. 1c, g-C$_3$N$_4$ NS exhibited layered morphology with some porous structures on its surface, which were created by ammonia-based gas bubbles during the thermal polymerization process of melamine [23], whereas RGO showed a flat and smooth layered morphology. Moreover, a close interfacial connection between the 2D g-C$_3$N$_4$ NS and RGO was observed, which is beneficial for fast charge transfer. The AFM image (Fig. 1d) showed that the size of RGO was approximately several micrometers and the thickness was around 0.5 nm, indicating a single layer structure according as previously reported [24]. The size of g-C$_3$N$_4$ NS was less than 1 μm and the thickness was 0.8 nm,

which suggested a double-layer structure. The total thickness of the g-C$_3$N$_4$ NS/RGO composite was about 1.4 nm. This ultra-thin 2D structure of the composite would provide short path and large contact area for charge transfer, which will endow the composite photocatalyst with efficient photogenerated charge separation [23].

The crystal structures of the as-prepared samples were examined by XRD. As shown in Fig. 2a, compared with bulk g-C$_3$N$_4$, the intensity of (002) peak at 27.5° (corresponding to the inter-planar stacking peak of conjugated aromatic systems) for the g-C$_3$N$_4$ NS became weaker, which indicated the layered structure of bulk g-C$_3$N$_4$ was exfoliated into nanosheets successfully. No characterized peak attributed to RGO was observed in the XRD spectrum of g-C$_3$N$_4$ NS/RGO composite, which may be because of the low content of RGO. To discern the presence of the RGO, Raman spectroscopy measurements of g-C$_3$N$_4$ NS and g-C$_3$N$_4$ NS/RGO were performed. The Raman spectrum of g-C$_3$N$_4$ NS displayed a broad peak from 1380 to 3000 cm^{-1}, which was mainly attributed to the overlap of several of peaks (N (N =C=N) at 1400 cm^{-1}, N (−CN) at 1600 cm^{-1}, N atmospheric stretching vibration at 2300 cm^{-1}, C (sp^2) at 1380 cm^{-1} and C (sp^3) at 1600 cm^{-1}) [25]. After loading RGO, the composite displayed two remarkable Raman peaks at 1340 and 1590 cm^{-1}, which was associated with the D and G bands, respectively (Fig. 2b). Further insights into the reduction of GO was obtained by FTIR (Fig. 2c). The peaks at 3000–3700 cm^{-1} and 1618 cm^{-1} of GO were attributed to those of −OH and C=O, respectively. The peaks ranged from 1406 to 1053 cm^{-1} were ascribed to C−O, C−OH and C−O−C. After the photoreduction process, all the peaks corresponding to the oxygen-containing functional groups were significantly reduced or negligible. This result suggests that the GO was successfully reduced into RGO during the photoreduction process. In addition, the expected functional groups in g-C$_3$N$_4$ NS were also obtained from the FTIR spectra. The broad peak at 3200 cm^{-1} and the multiple peaks in the 1600–1200 cm^{-1} region were ascribed to the N−H band and CN heterocycles, respectively. For the FTIR spectra of g-C$_3$N$_4$ NS/RGO composites, only the characteristic peaks of CN heterocycles in g-C$_3$N$_4$ NS appeared in the spectra, which was also because of the low content of RGO in the composite.

Light absorption is one of the crucial factors for photocatalysis especially the visible-light-driven photocatalysis. The UV–vis diffuse reflectance spectra of the samples were recorded and the results were showed in Fig. 2d. The absorption edge was around 430 nm for the g-C$_3$N$_4$ NS, indicating a band gap of 2.9 eV (Fig. S4). As for the g-C$_3$N$_4$ NS/RGO composite, although the absorption edge did not exhibit significant red-shift, the absorption intensity towards both UV light and visible light was enhanced, which was a typical behavior of RGO [26]. The PL spectra of both g-C$_3$N$_4$ NS/RGO and g-C$_3$N$_4$ NS were recorded to evaluate the efficiency of photogenerated charge separation for the photocatalysts. When the excitation wavelength was 380 nm, the emission peak appeared at about 430 nm for g-C$_3$N$_4$ NS (Fig. S5). This strong peak was attributed to the PL phenomenon with the energy of photons approximately equaling the band-gap energy of g-C$_3$N$_4$ NS. The g-C$_3$N$_4$ NS/RGO displayed a much lower PL intensity ($\approx$67% decrease) than that of g-C$_3$N$_4$ NS, which suggested that the recombination of photo-induced electron-hole pairs in the g-C$_3$N$_4$ NS/RGO composite was inhibited effectively. This result was attributed to the efficient photogenerated charge separation between g-C$_3$N$_4$ NS and RGO. RGO acted as an electron acceptor and it can accept the photogenerated electrons from the conduction band of g-C$_3$N$_4$ NS. Moreover, the large contact area and the short transfer distance between g-C$_3$N$_4$ NS and RGO made the photogenerated charge transfer easy. The efficient charge separation is beneficial for the enhancement of photocatalytic efficiency.
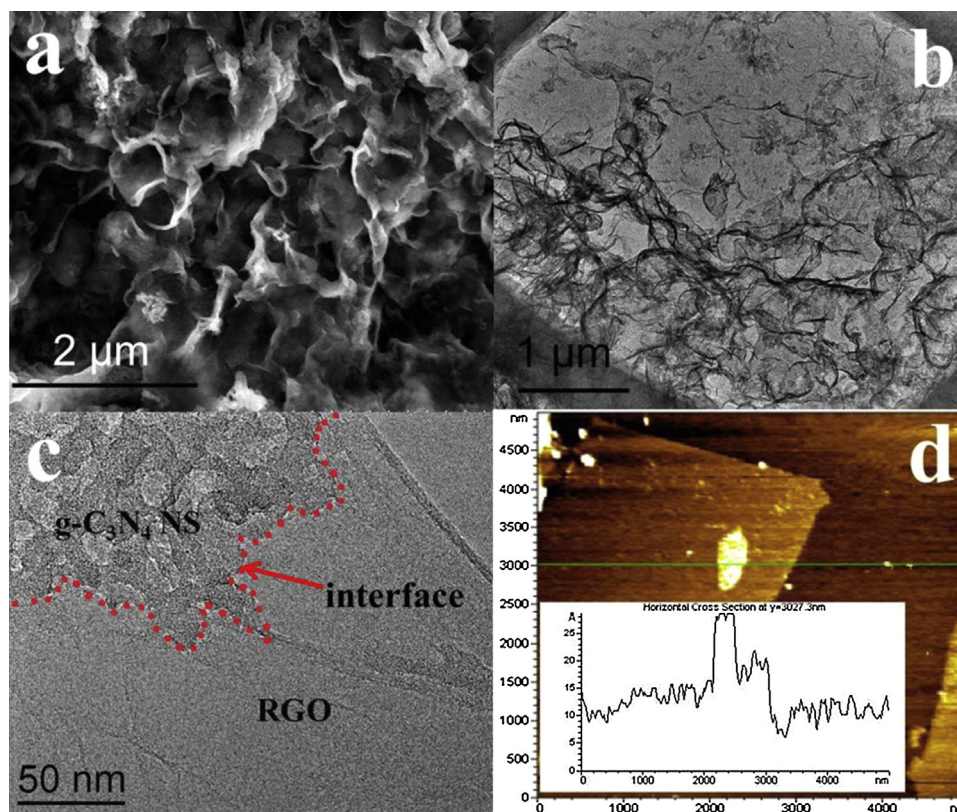
Fig. 1. Morphologies of the g-C$_3$N$_4$ NS/RGO composite: (a) SEM image; (b) TEM image; (c) high magnification of TEM image; (d) AFM image.
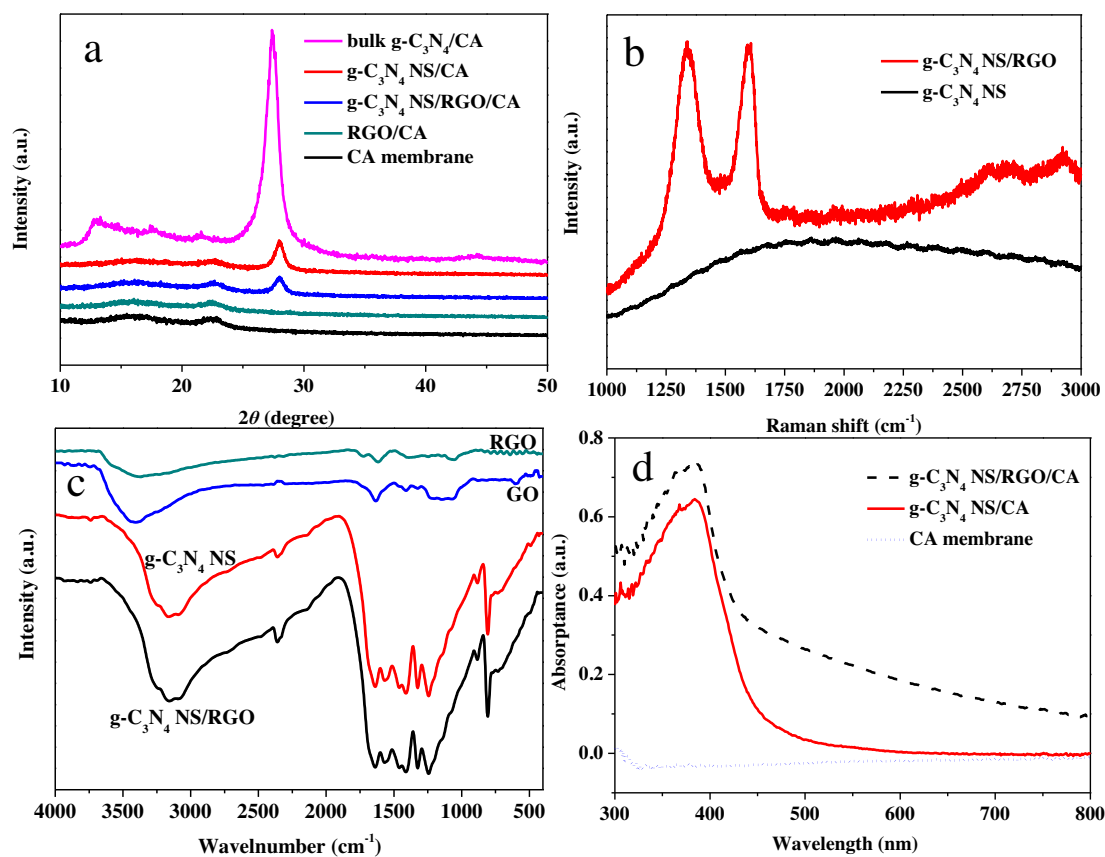

Fig. 2. (a) XRD patterns; (b) Raman spectra; (c) FTIR spectra; (d) UV–vis absorption.
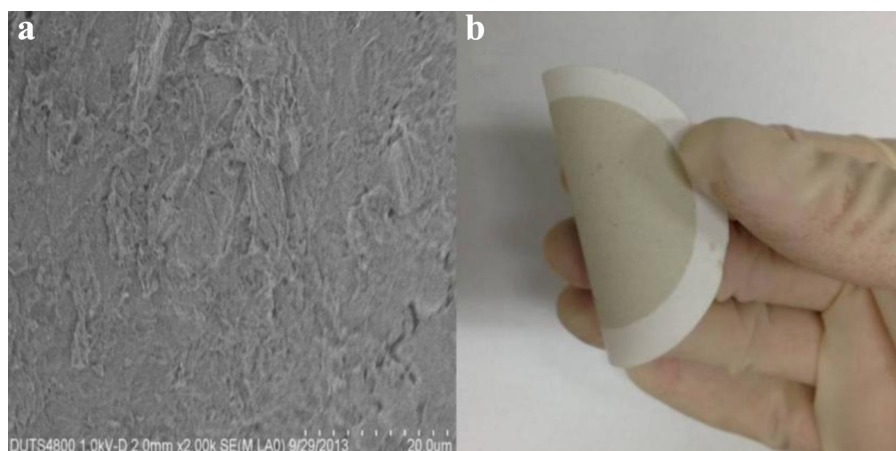
Fig. 3. (a) SEM image of the membrane surface; (b) digital photo of the g-C$_3$N$_4$ NS/RGO composite membrane.

3.2. Optimization of the photocatalytic functional layer

The content of RGO in g-C$_3$N$_4$ NS/RGO composite was crucial for efficient photocatalysis. To optimize the content of RGO in the composite, the photocatalytic efficiencies of the composites with different RGO contents for the degradation of RhB under visible light irradiation were evaluated. As shown in Fig. S6, the g-C$_3$N$_4$ NS/RGO composite photocatalysts with different RGO contents showed higher photocatalytic efficiencies than pure g-C$_3$N$_4$ NS. The degradation of RhB over g-C$_3$N$_4$ NS/RGO photocatalysts accords with pseudo first order kinetics by linear transforms ln (C$_0$/C$_t$) = kt. The kinetic constant of g-C$_3$N$_4$ NS/1% RGO was 4.83×10^{-2} min^{-1} (Fig. S7), which was four times as much as that of pure g-C$_3$N$_4$ NS. The enhanced photocatalytic activity was mainly due to the efficient photogenerated charge separation by RGO. A further increase in the content of RGO from 1 to 1.5 wt% led to a decrease of kinetic constant from 4.83×10^{-2} to 3.12×10^{-2} min^{-1}. The decrease of kinetic constant may be due to the introduction of an excess content of RGO that shielded g-C$_3$N$_4$ NS from light, weakening the light absorption by g-C$_3$N$_4$ NS. Thus, the g-C$_3$N$_4$ NS/RGO composite photocatalyst with 1 wt% RGO was chosen in the subsequent experiments.

Pure water flux measurements of g-C$_3$N$_4$ NS/RGO/CA membrane with different g-C$_3$N$_4$ NS/RGO deposited masses were carried out and the results are showed in Fig. S8. The flux of RGO/CA and P25/CA membranes decreased dramatically with increased deposited mass, indicating the decrease in effective pore size. Unlike RGO/CA and P25/CA membranes, whereby the flux did not decrease monotonically as the deposition mass increased, flux for the g-C$_3$N$_4$ NS/RGO/CA membrane was stable at 450 L m^{-2} h^{-1} with a 25 mg g-C$_3$N$_4$ NS/RGO assembly. We hypothesize that such flux can be attributed to the larger lateral size of g-C$_3$N$_4$ NS/RGO (>1 μm) than the pore sizes of CA membrane (0.45 μm), which prevent it from dropping into the pores. Moreover, the large number of channels offered by its crumpled morphology for water to permeate through. The composite membrane with 25 mg of photocatalyst deposition was chosen in the subsequent experiments.

3.3. Evaluation of membrane performance

The surface morphology of the composite membrane was observed by SEM. As shown in Fig. 3a, the surface of the membrane was coated by the g-C$_3$N$_4$ NS/RGO composite without visible cracks. The g-C$_3$N$_4$ NS/RGO/CA membrane remained flexible even after drying (Fig. 3b), whereas the pristine g-C$_3$N$_4$ NS/CA membrane without loading RGO displayed many creases, which was
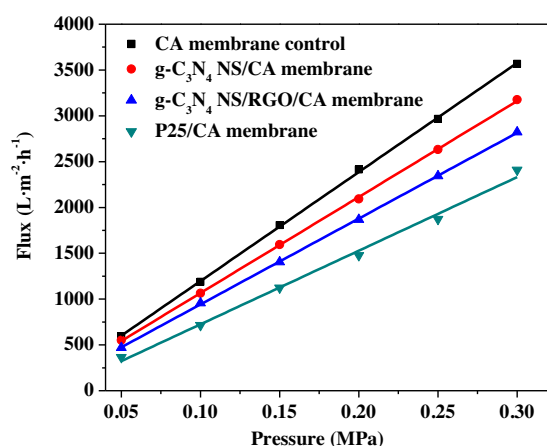

Fig. 4. Pure water flux of the membranes.

unfavorable for water filtration (Fig. S9). The enhanced flexibility was mainly attributed to the introduction of RGO which played an important role in connecting individual g-C$_3$N$_4$ NS. In addition, the membrane displayed good adhesion between photocatalyst and CA membrane substrate, which was illustrated by ultrasonic vibration tests (Fig. S10). No significant weight loss of photocatalyst occurred (less than 3%) within 30 min of ultrasonic vibration for the membrane. The good flexibility and mechanical strength was beneficial for the application of this membrane in practical water treatment.

The permeability and the separation property were evaluated by testing pure water flux and filtering PS microspheres, respectively. The permeation flux of each membrane was conducted in a dead-end membrane module. As shown in Fig. 4, a steady pure water flux of 957 L m^{-2} h^{-1} bar^{-1} for g-C$_3$N$_4$ NS/RGO/CA composite membrane was obtained, which was 33.8% higher than that of P25/CA membrane (715 L m^{-2} h^{-1} bar^{-1}). The flux increased linearly with the trans-membrane pressure, which indicated the pores formed by the creases of the g-C$_3$N$_4$ NS/RGO composite nanosheets were incompressible even under the high pressure (0.3 MPa). To evaluate the separation characteristics of the membrane, the rejection rates of PS microspheres with a series of diameters were measured. As illustrated in Fig. S11, more than 50% of 360 nm PS microspheres were rejected. When the diameter of PS microspheres increased to 430 nm, about 94% of microspheres were rejected, thus we conclude that the effective pore size of g-C$_3$N$_4$ NS/RGO/CA membrane was approximately 430 nm. Apart from the macropores of 430 nm, a hierarchical mesoporous structure was shown by BET measurements. According to the calculation from the desorption branch of
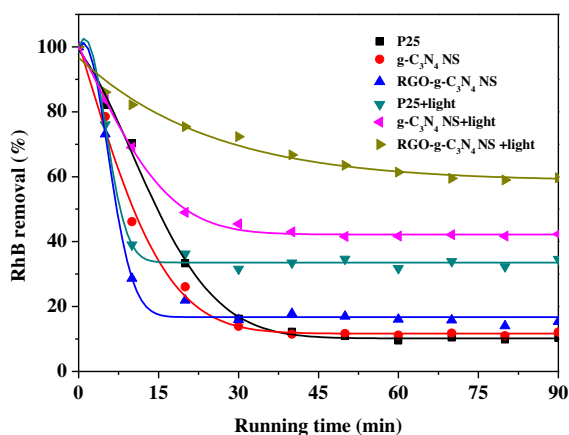
Fig. 5. Removal of RhB by different membranes under different conditions.

Fig. 6. *E. coli* removal under different conditions.

the isotherm by BJH model, the mesopores of g-C_3N_4 NS/RGO composite ranged from 2 to 30 nm with a peak around 3.8 nm (Fig. S12). The formation of mesopores may be because of the wrinkles and the 2D channels between the stacked nanosheets [27,28]. The mesoporous structure provides more channels for water permeation and expose more active sites for photocatalytic reaction [29].

3.4. Removal of RhB by the membrane

RhB is an organic contaminant and one of the most widely used industrial dyes. RhB is always involved in industrial wastewater with biorefractory, high COD, high chromaticity and toxicity. The molecular size of RhB is $1.44 \times 1.09 \times 0.64$ nm, which makes it difficult to remove by traditional microfiltration through size-exclusion. However, owing to the excellent photocatalytic performance on degradation of RhB (Fig. S13), the composite membrane may exhibit good performance for removing it. As shown in Fig. 5, only 15% of RhB was removed using membrane separation alone, whereas for the integrated process, the removal rates were increased. More than 60% of RhB was removed by the integrated process for the g-C_3N_4 NS/RGO/CA membrane, which was four times that of filtration alone for the same membrane. The enhanced removal rate was mainly attributed to the photocatalytic degradation towards organic contaminants. Also, the removal rate on g-C_3N_4 NS/RGO/CA membrane was higher than that of P25/CA (32%) and g-C_3N_4 NS/CA membrane (45%), which was attributed to the high photocatalytic efficiency of g-C_3N_4 NS/RGO among them. Apart from RhB, BPA which is a typical endocrine disrupter, was also used as a model contaminants to evaluate the membrane performance. The removal rate of BPA for the g-C_3N_4 NS/RGO/CA membrane under visible light irradiation was 22% higher than that of filtration alone. (Fig. S14).

3.5. Inactivation and antifouling performance

As well as organic contaminants, microbial pollution has attracted much attention because of the health risks involved. Because the typical sizes of the bacterial cells range from 0.2 to 5 μm, the complete removal of bacterial is still a challenge for the g-C_3N_4 NS/RGO/CA microfiltration membrane because the effective rejection size is 430 nm. Moreover, biofouling is another obstacle for the membrane during the filtration process, which will lead to a high permeate loss [30]. However, these problems are expected to be solved partially by the integrated process using photocatalytic membranes. In this study, *E. coli*, as a common microorganism was chosen as a representative waterborne pathogen to evaluate the inactivation and antifouling performance of the membrane in the
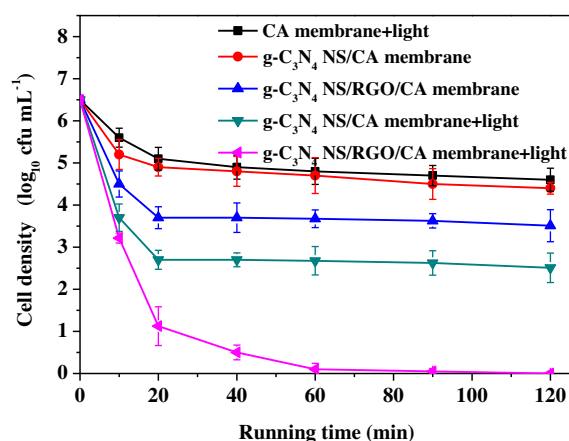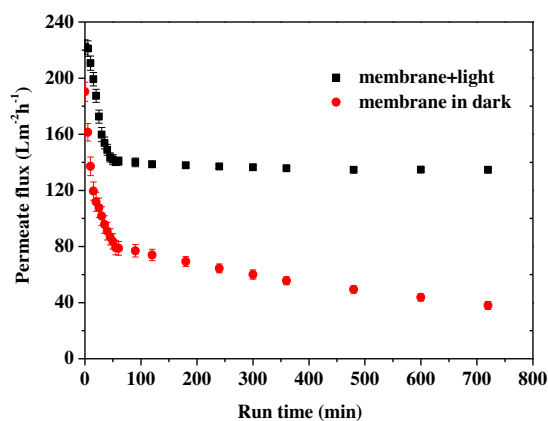

Fig. 7. Anti-fouling property of the composite membrane under filtration with and without visible light irradiation.

integrated process. The removal of *E.coli* in an integrated process by the composite membrane may result from two processes: the rejection by the membrane and inactivation by photocatalysis. As shown in Fig. 6, for the process of membrane separation alone, about three log units of *E. coli* were rejected by the g-C_3N_4 NS/RGO/CA membrane. For the integrated process using the same membrane, more than six log units of *E. coli* were removed. The increment of the *E. coli* removal was contributed to the inactivation via photocatalysis. To confirm the complete removal of *E. coli* after treatment by g-C_3N_4 NS/RGO/CA membrane under the integrated process, a fluorescent microscopic measurement was carried out (Fig. S15). The viable cells accumulated 4′,6-diamidino-2-phenylindole appearing blue under a fluorescent microscope. No viable cells with blue color were observed for g-C_3N_4 NS/RGO/CA membrane in the integrated process, which indicated no *E. coli* survived in the effluent based on our detection limits.

The permeation flux of the g-C_3N_4 NS/RGO/CA membrane with and without visible light irradiation during the *E. coli* removal process were measured to investigate the antifouling performance resulting from the visible-light-driven photocatalysis. As shown in Fig. 7, the permeation flux was initially declined as the running time increased and was stable after 1 h. For the g-C_3N_4 NS/RGO/CA membrane under visible light irradiation, the stable permeation flux was 140 L m^{-2} h^{-1} which was 3.7 times that of filtration in dark (38 L m^{-2} h^{-1}). The enhancement of the permeation flux was probably due to two aspects: (1) destruction of bacteria foulants formed on the surface of membrane via photocatalysis. (2) diminution of

Table 1
Water quality of the surface water.

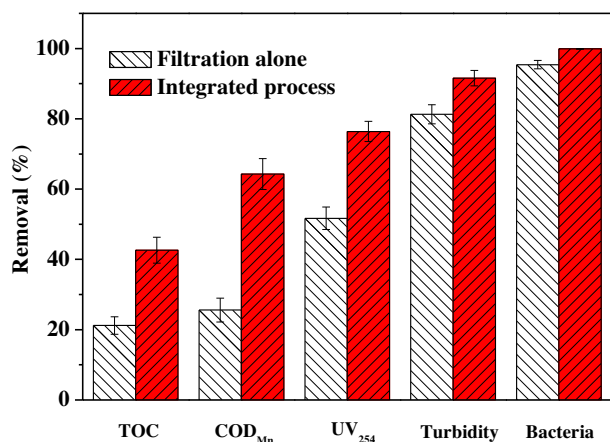| Item	Average value	deviation range
COD_{Mn} (mg L^{-1})	1.1	± 0.5
TOC (mg L^{-1})	8.2	± 0.6
Total colony counts (cfu L^{-1})	1.0×10^3	$\pm 5 \times 10^2$
UV_{254} (cm^{-1})	0.084	± 0.006
Turbidity (NTU)	2.6	± 0.3
pH	7.1	± 0.2

Fig. 8. The contaminants removal from surface water by g-C_3N_4 NS/RGO/CA membrane.

bacterial attachment on the membrane because of the reactive oxygen species produced by photocatalysis [31].

3.6. Surface water treatment

To evaluate the performance of the integrated process using g-C_3N_4 NS/RGO/CA membrane in real surface water treatment, we collected surface water from a reservoir near Dalian city. The typical items of water quality for the surface water are shown in Table 1. The water treatment was conducted in a continuous flowing mode. The experimental results were shown in Fig. 8. For the membrane separation process, the removal rates of turbidity and bacteria were 84% and 97%, respectively. For comparison, more than 90% of the turbidity and nearly all the bacteria were removed by the integrated process. Benefiting from the photocatalytic degradation of organic contaminants, the integrated process exhibited higher performance than that of membrane separation alone on organic pollutants removal. Removal of TOC, COD_{Mn} and UV_{254} were only 21%, 25% and 52%, respectively, for the membrane separation alone and reached 42%, 64% and 78% for the integrated process, respectively. The result showed clearly the superior performance of the integrated process of membrane separation and visible-light-driven photocatalysis using g-C_3N_4 NS/RGO/CA membrane compared with the process of membrane filtration alone.

4. Conclusion

In summary, a novel g-C_3N_4 NS/RGO/CA microfiltration membrane was successfully fabricated by a vacuum filtration method.

Owing to the attractive photocatalytic efficiency of g-C_3N_4 NS under visible light irradiation and photogenerated charge separation resulting from the unique hetero-structure between g-C_3N_4 NS and RGO, the g-C_3N_4 NS/RGO/CA composite photocatalytic membrane exhibited high performance for the removal of organic contaminants and complete bacterial inactivation in the integrated process of filtration with visible light photocatalysis. Membrane fouling was mitigated significantly in the integrated process. All advantages shown by the composite photocatalytic membrane make it promising for water treatment application.

Acknowledgements

Appendix A. Supplementary data

Supplementary data associated with this article can be found, in the online version, at http://dx.doi.org/10.1016/j.apcatb.2016.04.042.

References

[1] D.W. Kolpin, E.T. Furlong, M.T. Meyer, E.M. Thurman, S.D. Zaugg, L.B. Barber, H.T. Buxton, Environ. Sci. Technol. 36 (2002) 1202–1211.
[2] M. Elimelech, W.A. Phillip, Science 333 (2011) 712–717.
[3] G. Owen, M. Bandi, J. Howell, S. Churchouse, J. Membr. Sci. 102 (1995) 77–91.
[4] H. Huang, K. Schwab, J.G. Jacangelo, Environ. Sci. Technol. 43 (2009) 3011–3019.
[5] B.K. Pramanik, F.A. Roddick, L. Fan, J. Membr. Sci. 475 (2015) 147–155.
[6] W. Wang, A. Irawan, Y. Ku, Water Res. 42 (2008) 4725–4732.
[7] S. Mozia, D. Darowna, A. Orecki, R. Wrobel, K. Wilpiszewska, A.W. Morawski, J. Membr. Sci. 470 (2014) 356–368.
[8] N.H. Lee, G. Amy, J.P. Croue, H. Buisson, Water Res. 38 (2004) 4511–4523.
[9] H. Zhang, X. Quan, S. Chen, Environ. Sci. Technol. 40 (2006) 6104–6109.
[10] H. Choi, A.C. Sofranko, D.D. Dionysiou, Adv. Funct. Mater. 16 (2006) 1067–1074.
[11] H. Choi, E. Stathatos, D. Dionysiou, Appl. Catal. B: Environ. 43 (2006) 60–67.
[12] L. Liu, Z. Liu, H. Bai, Water Res. 46 (2012) 1101–1112.
[13] X. Wang, K. Maeda, A. Thomas, Nature Mater. 8 (2009) 76–80.
[14] S. Yan, Z. Li, Z. Zou, Langmuir 26 (2010) 3894–3901.
[15] J. Mao, T.Y. Peng, X.H. Zhang, K. Li, L.Q. Ye, L. Zan, Catal. Sci. Technol. 3 (2013) 1253–1260.
[16] H. Zhao, H. Yu, X. Quan, S. Chen, H. Zhao, H. Wang, RSC Adv. 4 (2014) 624–628.
[17] J. Xu, L. Zhang, R. Shi, Y. Zhu, Mater. Chem. A 1 (2013) 14766–14772.
[18] H. Zhang, X. Fan, X. Quan, S. Chen, H. Yu, Environ. Sci. Technol. 45 (2011) 5731–5736.
[19] P. Niu, L. Zhang, G. Liu, H.M. Cheng, Adv. Funct. Mater. 22 (2012) 4763–4770.
[20] H.M. Zhang, H.J. Zhao, P.R. Liu, S.Q. Zhang, G.Y. Li, J. Membr. Sci. 343 (2009) 212–218.
[21] Y. Hou, X. Li, Q. Zhao, Environ. Sci. Technol. 46 (2012) 4042–4050.
[22] S. Li, S. Gu, W. Liu, H. Han, Q. Zhang, China Catena 75 (2008) 216–222.
[23] Y. Hou, Z. Wen, S. Cui, Adv. Mater. 25 (2013) 6291–6297.
[24] K.S. Novoselov, A.K. Geim, S. Morozov, D. Jiang, Y. Zhang, S. Dubonos, I. Grigorieva, A. Firsov, Science 306 (2004) 666–669.
[25] S. Yang, Y. Gong, J. Zhang, L. Zhan, L. Ma, Z. Fang, R. Vajtai, X. Wang, P.M. Ajayan, Adv. Mater. 25 (2013) 2452–2456.
[26] P. Gao, Z. Liu, M. Tai, Appli. Catal. B: Environ. 17-25 (2013) 138–139.
[27] M. Hu, B. Mi, Environ. Sci. Technol. 47 (2013) 3715–3723.
[28] Y. Han, Z. Xu, C. Gao, Adv. Funct. Mater. 23 (2013) 3693–3700.
[29] J. Du, X. Lai, N. Yang, ACS Nano 5 (2011) 590–596.
[30] J. Chalor, A. Gary, Environ. Sci. Technol. 40 (2006) 969–974.
[31] N. Ma, X. Fan, X. Quan, J. Membr. Sci. 336 (2009) 109–117.